Toward Sustainable Tackling of Biofouling Implications and Improved Performance of TFC FO Membranes Modified by Ag-MOF Nanorods

Original
Toward Sustainable Tackling of Biofouling Implications and Improved Performance of TFC FO Membranes Modified by Ag-MOF Nanorods / Seyedpour, S. F.; Dadashi Firouzjaei, M.; Rahimpour, A.; Zolghadr, E.; Arabi Shamsabadi, A.; Das, P.; Akbari Afkhami, F.; Sadrzadeh, M.; Tiraferri, A.; Elliott, M.. - In: ACS APPLIED MATERIALS & INTERFACES. - ISSN 1944-8252. - 12:34(2020), pp. 38285-38298. [10.1021/acsami.0c13029]

Availability:
This version is available at: 11583/2846961 since: 2020-09-29T10:46:01Z

Publisher:
American Chemical Society

Published
DOI:10.1021/acsami.0c13029

Toward Sustainable Tackling of Biofouling Implications and Improved Performance of TFC FO Membranes Modified by Ag-MOFs Nanorods

S. Fatemeh Seyedpour[1,a], Mostafa Dadashi Firouzjaei[1,b,c], Ahmad Rahimpour[a]*, Ehsan Zolghadr[d], Ahmad Arabi Shamsabadi[e], Parnab Das[c], Farhad Akbari Afkhami[f], Mohtada Sadrzadeh[g], Alberto Tiraferri[h], and Mark Elliott [c]*

[a] Department of Chemical Engineering, Babol Noshirvani University of Technology, Shariati Ave., Babol, 4714781167, Iran
[b] Department of Chemical and Biological Engineering, University of Alabama, Tuscaloosa, AL 35487, USA
[c] Department Civil, Environmental and Construction Engineering, University of Alabama, Tuscaloosa, AL, 35487, USA
[d] Department of Physics and Astronomy, University of Alabama, Tuscaloosa, AL, 35487, USA
[e] Department of Chemistry, University of Pennsylvania, Philadelphia, Pennsylvania 19104, USA
[f] Department of Chemistry, The University of Alabama, Tuscaloosa, AL 35487, United States
[g] Department of Mechanical Engineering, 10-367 Donadeo Innovation Center for Engineering, Advanced Water Research Lab (AWRL), University of Alberta, Edmonton, AB, T6G 1H9, Canada
[h] Department of Environment, Land and Infrastructure Engineering (DIATI), Politecnico di Torino, Corso Duca degli Abruzzi 24, 10129 Turin, Italy

*Corresponding authors:

Ahmad Rahimpour (ahmadrahimpour@nit.ac.ir)

Mark Elliott (melliott@eng.ua.edu)

[1] The authors contributed equally to this work.

ABSTRACT

In this work, nanorods with highly antibacterial properties were synthesized using silver acetate as a metal source and 2-aminoterephthalic acid as an organic linker, and were then incorporated into thin-film composite membranes to improve their performance as well as to alleviate biofouling. Silver metal-organic frameworks (Ag-MOFs) nanorods with a length smaller than 40 nm were embedded within the polyamide selective layer of the membranes during interfacial polymerization. The interaction of the synthesized nanorods with the polyamide was favored on account of the presence of amine-containing functional groups on the surface of the nanorods. The results of X-ray photoelectron spectroscopy, field emission scanning electron microscopy, energy-dispersive X-ray spectroscopy, and atomic force microscopy characterizations proved the presence of Ag-MOFs nanorods in the selective layer of the thin-film nanocomposite (TFN) membranes. TFN membranes demonstrated improved water permeance and salt selectivity, and superior antimicrobial properties. Specifically, the increased hydrophilicity and antibacterial activity of the TFN membranes led to a synergetic effect toward biofouling mitigation. The number of live bacteria attached to the surface of the neat TFC membrane decreased by more than 92% when a low amount of Ag-MOFs nanorods (0.2 wt%) was applied. Following contact of the TFN membrane surface with *E. coli*, full inactivation and degradation of bacteria cells were observed with microscopy, colony-forming unit tests, and disc inhibition zone analyses. This result translated to a negligible amount of biofilm formed on the active layer. Indeed, the incorporation of Ag-MOFs nanorods decreased the metal ion release rate and therefore provided prolonged antibacterial activity.

Keywords: Forward osmosis; Thin-film nanocomposite membranes; Ag-MOFs nanorods; antibacterial activity; biofouling mitigation.

INTRODUCTION

Thin-film composite (TFC) polyamide (PA) membranes are widely applied in forward osmosis and desalination processes, as they currently provide the best combination of water flux and salt rejection. [1] However, the high susceptibility of polyamide-based membranes to biofouling, owing to their relatively high hydrophobicity, surface roughness, and the presence of carboxyl groups, is the most significant challenge to the achievement of cost-effective operations of water desalination processes. [2] Since the surface properties dictate the interactions between foulants and the membrane, the vast majority of recent studies have focused on innovative strategies to prevent foulant attachment and to increase membrane lifespan. [3] Various approaches have been implemented, including physical surface coating, chemical functionalization, and in-situ growth or incorporation of nanoparticle (NPs) within the polyamide layer. [4-5] Embedding NPs within the polyamide layer with the aim of fabricating thin-film nanocomposite (TFN) membranes presents specific advantages over other methods, including facile fabrication method and water flux enhancement [6]. [7]

The incorporation of NPs into the polyamide layer during the interfacial polymerization (IP) reaction is also a feasible approach to obtain membranes with customized characteristics, such as fouling resistance. [8] The final performance of the TFN membrane can be virtually tuned by designing NPs with specific properties and applying them during the IP procedure. [9] The first effort to fabricate TFN membranes for water treatment was reported in 2005 using zeolite-A as the nanofiller. Since then, diverse types of NPs, including carbon-based nanomaterials (*e.g.*, carbon nanotube and graphene oxide), minerals (*e.g.*, zeolite, titania, and silica), and metals and metal oxides (*e.g.*, silver, copper, and zinc oxide) have been utilized to develop TFN membranes. Despite significant advances in fabrication of robust TFN membranes by effective incorporation of NPs into the polyamide layer, there are still bottlenecks that need to be tackled, including (i) the poor interaction of the NPs with the surrounding polyamide matrix, which increases the release of NPs during filtration and accordingly reduces their activity over time, [8, 10] (ii) the inappropriate compatibility between the NPs and surrounding polyamide matrix, which adversely affect the membrane selectivity, [8] (iii) the improper size and morphology of NPs, which affect the polyamide selective layer mechanical strength and integrity, [11] (iv) the inhomogeneous dispersion of the NPs in the solution during the IP process and in the final polyamide layer, and (vi) the difficulty of NPs synthesis and hence TFN membrane fabrication for large-scale applications. [12] Metal-organic frameworks [13] (MOFs) are one of the alternative materials proposed to address these bottlenecks. [14]

Due to the presence of the organic linker in their structures, MOFs provide higher affinity and improved compatibility with the polyamide chain, in comparison to their fully inorganic counterparts. This greater interaction between the two components at the MOF-polymer interface can be related to covalent, non-covalent, and hydrogen bonds, which indeed prevent the formation of non-selective voids (*i.e.*, defects) between the phases. [8] Additionally, MOFs are widely reported for their antibacterial activity in the literature, as a source of metal ions with the potential for controlled release of biocidal agents. [15] The homogenous distribution of active metal centers in their frameworks offers a prolonged biocidal activity without aggregation or oxidation. [15] Despite being reported in the literature for the fabrication of the TFN membranes, few studies have achieved a suitable membrane functionalization without compromising membrane performance, and fewer have reported the biofouling behavior in the FO process. [16]

The main objectives of this study are: (i) promoting interaction and compatibility between the polyamide matrix and the MOFs to improve their incorporation within the TFN membranes, (ii) improving surface hydrophilicity by introducing Ag-MOFs nanorods to minimize foulant deposition onto the membrane, (iii) introducing desirable charged moieties to exert electrostatic repulsion with bio-foulants, and (iv) acheving high antimicrobial activity and long-lasting antibiofouling properties for TFN membranes with a simple approach. In this regard, we address the TFN membrane challenges by synthesizing and incorporating novel Ag-MOFs nanorods with a length of 30-40 nm. Two approaches are investigated, whereby Ag-MOFs nanorods are dispersed in the 1,3-phenylenediamine (MPD) aqueous solution or in the trimesoylchloride (TMC) organic phase during the IP reaction. The potential influence of Ag-MOFs nanorods on the morphologies and surface hydrophilicity, as well as the chemistry of the TFN membranes, are systematically investigated. The antifouling performance is evaluated by conducting fouling experiments using alginate and *E. coli* as model organic and bio-foulants, respectively. Finally, the antibacterial properties of the membrane are extensively studied via a combination of complementary techniques.

MATERIALS & METHODS

Reagents. Polyethersulfone (PES, Ultrason E6020P, M_W = 58,000 g/mol) as polymer, N, N-dimethylformamide (DMF 99.5%, Scharlau) as solvent, and Triton X-100 (Merck) and polyvinylpyrrolidone (PVP, M_W = 25,000 g/mol, Merck) as pore formers were used for the preparation of the casting solutions to fabricate the support layer of FO membranes. Trimesoylchloride (TMC, Merck), 1,3-phenylenediamine (MPD, Merck), triethylamine (TEA, Merck), camphorsulfonic acid (CSA, Merck), and n-hexane (99%, Scharlau) were used for the synthesis of the polyamide selective layer by IP reaction. Sodium chloride (NaCl, 99.5%, Merck) was used as a draw solute (DS) at different concentrations in FO filtration experiments. Silver acetate (≥ 98.0 %, Merck), and 2-aminoterephthalic acid (NH_2-BDC, ≥ 95.0 %, Sigma Aldrich) were used for the synthesis of Ag-MOFs nanorods. Potassium dihydrogen phosphate (KH_2PO_4, 99.5%), glucose monohydrate, magnesium sulfate ($MgSO_4.6H_2O$, 99%), sodium bicarbonate ($NaHCO_3$, 99.5%), calcium chloride ($CaCl_2$, 96%), and ammonium chloride (NH_4Cl, 99.5%) were purchased from Merck and used for the preparation of synthetic wastewater feed solutions. Sodium alginate was purchased from Sigma-Aldrich and used a representative organic foulant.

Synthesis and Characterization of Ag-MOFs Nanorods. A solution of silver acetate (0.2 g) in 100 mL of deionized water was gradually added to the NH_2-BDC solution (0.1 g dissolved in 100 mL of ethanol), while stirring slowly at 100 rpm, to form a precipitate after the synthesis reaction. Prior to the synthesis, both solutions were sonicated for 5 min to obtain homogenous solutions without any agglomeration. The final mixture was stirred for 30 min to complete the reaction, after which the precipitate was filtered and washed twice with 100 mL of ethanol to remove the unreacted reagents and then dried at 60 °C. The sample was then analyzed using Fourier transform infrared (FTIR) and energy-dispersive X-ray (EDX) spectroscopic analyses to confirm the successful formation of Ag-MOFs nanorods. The morphology of Ag-MOFs nanorods was observed using field emission scanning electron microscopy (FESEM, TESCAN MIRA3) equipped with an EDX spectrometer.

Preparation of the Neat TFC and the TFN Membranes. The PES support membrane was fabricated via a non-solvent induced phase separation method. [8] The TFC membranes were fabricated on the PES surface through an IP reaction involving MPD aqueous and TMC organic solutions. [8] The TFC polyamide membrane (M0) was prepared by soaking the PES substrate in an aqueous solution containing 2 wt% MPD, 2 wt% CSA, and 1 wt% TEA for 2 min. The excess MPD solution was then carefully removed from the membrane surface by an air-knife. The amine-saturated membrane was then immersed in a 0.1 wt/v% TMC solution (n-hexane solvent) for 30 s. Subsequently, the membrane was placed inside a pre-heated oven at 80 °C for 5 min to complete the formation of an ultrathin polyamide selective layer. The TFN membranes were prepared by suspending Ag-MOFs nanorods (0.2 wt%) into the aqueous MPD solution (M1) or into the organic TMC solution (M2) during the IP process. Before use, these solutions containing the Ag-MOFs nanorods were sonicated for 20 min to prevent any undesired agglomeration. All the membranes were stored in 20 °C deionized water before testing or characterization.

Membrane Surface Characterization. FESEM (MIRA3 TESCAN) equipped with an EDX detector was applied to characterize the surface and cross-sectional morphologies of the membranes. Atomic force microscopy (AFM, EasyScan II, Swiss) was used to determine the surface roughness of the membrane samples. To minimize the experimental error, the surface roughness was determined for three separately cast membranes. The surface chemistry of the membranes was analyzed by attenuated total reflectance-FTIR (ATR-FTIR, Thermo Scientific USA). The surface charge of both neat TFC (M0) membrane, as well as M1 and M2 TFN membranes, was assessed with a SurPASS electrokinetic solid surface zeta potential analyzer (Anton Paar USA, Ashland, VA). All the streaming potential measurements were conducted in a background electrolyte solution composed of 1 mM KCl at 25 °C over a pH range 4-9. The zeta potentials of the membranes were calculated based on the Helmholtz-Smoluchowski equation. Two separate samples of each membrane were assessed to minimize experimental error. The membrane surface hydrophilicity was assessed by means of contact angle measurements (Dataphysics, OCA 15 plus), where an average value was calculated from measurements at five random positions. The elemental composition and chemical bonding information of the membrane surface, as well as the release of silver ions from the membrane structure were evaluated by X-ray photoelectron spectroscopy (XPS, Bestec, Germany) and inductively coupled plasma-optical emission spectrometry (ICP-OES, Varian 730-ES), respectively.

Evaluation of the Membrane Permeation Properties. The transport properties of all the membranes were evaluated in terms of water permeability coefficient (A) and salt permeability coefficient (B) with a cross-flow filtration unit with an effective membrane active area of 30 cm^2. [8] DI water and NaCl were used as feed and draw solutions, respectively, in FO filtration experiments. Further information on the FO setup and the performance evaluation procedure are reported in the Supporting Information (SI.1.1). [17]

Dynamic Fouling Experiments. The organic fouling and biofouling propensity of the FO membranes were assessed by adding sodium alginate (a model polysaccharide) and *E. coli* (model bacteria), respectively, in the feed solutions during FO filtration experiments. Further details on the fouling experiments are provided in the Supporting Information (section 1.2). [8, 18]

Fluorescent Scanning Microscopy. *E. coli* was used for Epi-fluorescence microscopy. Epi-fluorescence scheme was used for the fluorescence imaging. In each experiment, 1 mL of the stock bacterial suspension was placed onto a 1×1 cm^2 membrane sample; viability staining was performed after 1 h of contact. The SYTO9-stained bacteria (green) and PI-stained bacteria (red) corresponded to live and the dead cells, respectively. Further details on the fluorescence imaging procedures are presented in the Supporting Information (section 1.3).

Heterotrophic Plate Count. The *E. coli* bacteria were grown at 37 °C in trypticase soy broth (TSB) with incubation and shaking overnight. After this period, a fresh broth sample was incubated with some of the bacterial TSB suspension for 3 h at 37 °C. By centrifuging for 2 min at 6000 rpm, the bacterial culture was then fully pelletized. The resulting bacterial solution was suspended again in 1X sterile phosphate buffer saline (PBS) solution to achieve a final concentration of 10^7 colony-forming unit (CFU)/mL. Membrane samples with the surface area of a 4 cm^2 were incubated at 37 °C in a sterile petri dish containing the bacterial solution under continuous mild shaking for 1 h. The unattached bacterial cells were removed by rinsing the membrane samples three times with a PBS solution. To re-suspend the attached bacteria, membrane samples were then placed in a sterile plastic bag with 10 mL of PBS stock solution and sonicated for 7 min. The resulting solution was poured onto previously-prepared TSB agar plates after series dilutions; the plates were finally incubated for 24 h at 37 °C, and the CFU was finally counted. [19]

Disc Inhibition Zone Assay. To further investigate the antimicrobial properties of the membranes, a disc inhibition zone assay was performed to determine the inhibition zone of all the membranes. [20] TSB (5 mL) was poured inside Petri dishes and solidified in a biosafety cabinet. The plates were incubated at 37 °C for 24 h to eliminate any plates with contamination. *E. coli* fresh suspensions were obtained as described above. A sterile cotton swab was then dipped into the *E. coli* suspension and was spread on the agar plates. The membranes were cut into 6-mm diameter discs, which were placed in the middle of the agar plates already inoculated with *E. coli*. The plates were then incubated (without shaking) for 24 hours at 37 °C.

RESULTS & DISCUSSION

Characteristics of Ag-MOFs nanorods and proposed interaction with polyamide. Figure 1a illustrates the schematic structure of Ag-MOF nanorods. To confirm the successful synthesis of the nanorods, a thorough morphological and physicochemical characterization was conducted. As illustrated in **Figure 1b, c**, the FESEM micrographs of the as-prepared Ag-MOF samples demonstrated the narrow size distribution of nanorods within the range of 30-40 nm. **Figure 1d-g** presents EDX mapping of carbon, nitrogen, oxygen, and silver atoms on Ag-MOF nanorods. The elemental EDX composition of Ag-MOF nanorods **(Figure 1h)** indicated 27.54 % and 10.16 % of silver and nitrogen, respectively. The infrared absorption peaks observed in the IR spectrum of **Figure 1i** can be summarized as follows: the broad peak centered around 3300 cm^{-1} is the fingerprint for O–H stretching. [21] The observed peak at 1544 cm^{-1} is attributed to C–N stretching and also N–H bending. [14, 22] Additionally, N–H stretching is observed at 1610 cm^{-1}. [22] The two peaks at 1355 and 1410 cm^{-1} most likely correspond to C=C and C=O stretching, respectively. The peak at 1240 cm^{-1} is due to C–O–C symmetric stretching. [23] Moreover, the peak at 1031 cm^{-1} is related to C–O stretching. [24-25] Besides, several peaks in the range of 824-688 cm^{-1} may be assigned to C–H bonding, especially rocking vibrations. [23, 25] The more subtle peaks between 500 and 577 cm^{-1} can be associated with Ag–O vibrations. [26]

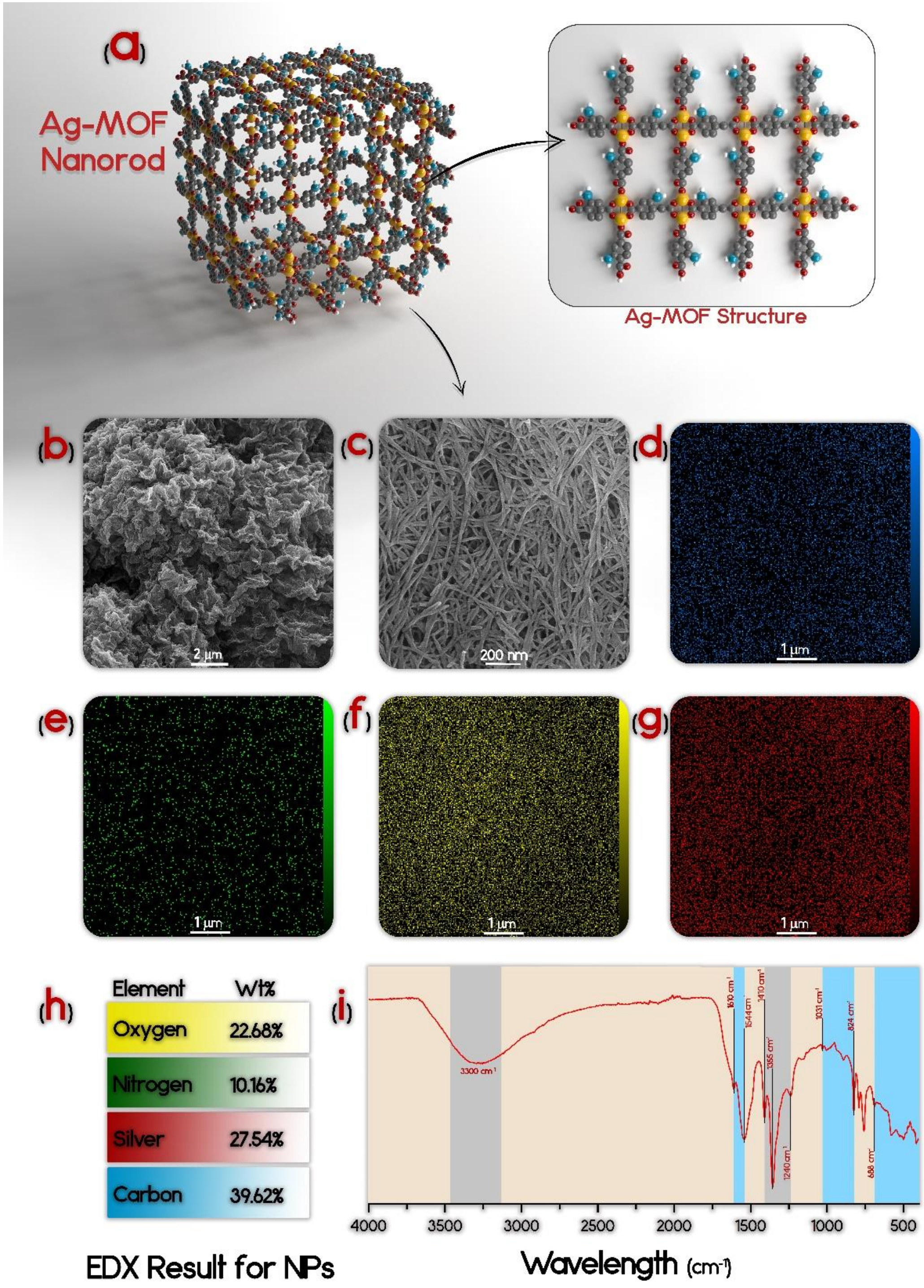

Figure 1. a) Schematic illustration of Ag-MOF structure (yellow: silver, grey: carbon, blue; nitrogen, red: oxygen, white: hydrogen); b and c) representative FESEM micrographs of Ag-MOF nanorods; EDX mapping of d) carbon, e) nitrogen, f) oxygen, g) silver on Ag-MOF nanorods; h) elemental EDX composition of Ag-MOF nanorods; and i) FTIR spectrum of the as-prepared Ag-MOFs nanorods.

As with all other nanomaterials, incorporation of MOFs influences the polyamide-based layer structure, as nanostructures may change the kinetics of IP reaction, interact with the polyamide matrix, and may alter the degree of acid chloride hydrolysis. [27] Indeed, the penetration rate of MPD/TMC monomers into the reaction zone may alter during the IP process, and usually a looser polyamide layer forms. In this study, both the aqueous MPD and the organic TMC solutions underwent a color change upon the introduction of the Ag-MOFs, which was more intense in the case of MPD solution, whereby its color turned rapidly from transparent to black. [28] The amine functional groups present on the surface of Ag-MOFs nanorods most likely interacted with MPD and/or TMC molecules before and during the IP process, thus influencing the rate of the polycondensation reaction between amine and acyl chloride monomers and the final polyamide structure. The amino groups of Ag-MOFs nanorods can form covalent bonds with TMC monomers; whereas they interact with diamine-containing MPD monomers via hydrogen bonds. Both types of interactions improved the dispersion and compatibility of MOFs in the polyamide matrix. [29-30] **Figure 2** presents a schematic of possible interaction between Ag-MOFs nanorods and the polyamide chains during the IP process. A further schematic of the aqueous MPD and organic TMC solutions immediately after the introduction of Ag-MOFs nanorods at ambient temperature are presented in the Supporting Information (Figure S1).

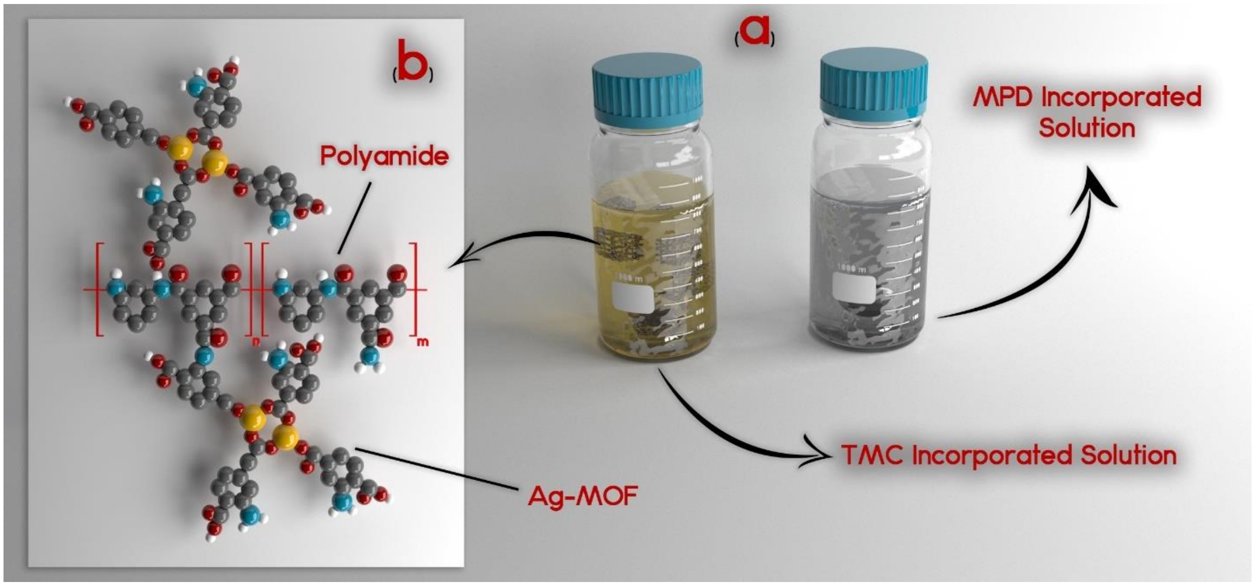

Figure 2. (a) Graphic illustration of the aqueous MPD and organic TMC solutions immediately after addition of Ag-MOFs nanorods; (b) proposed mechanism of interaction between the Ag-MOFs nanorods and the polyamide matrix in which the active sites of both hydrogen and covalent bonds are defined (yellow: silver; grey: carbon; blue: nitrogen; red: oxygen; white: hydrogen).

ATR-FTIR spectroscopy was performed to characterize the membrane surface functional groups and to further verify the successful binding of Ag-MOFs nanorods (**Figure 3**). The broad peak centered around 3300 cm^{-1} represents the O–H stretching. [21] The peaks over the wavenumbers of 1150-1320 cm^{-1} are related to PES support and are identified in all membranes due to the high penetration depth of the IR beam (>300 nm). [31] The peaks at 1150 cm^{-1} can be attributed to the symmetric O=S=O stretching vibration of the sulfone group. The peaks around 1300 cm^{-1} and 1320 cm^{-1} corresponded to the doublet from the asymmetric O=S=O stretching vibration and 1240 cm^{-1} to the asymmetric C–O–C stretching vibration of the aryl ether group of the PES support layer, respectively. [32] The peaks of the polyamide layer formed by IP process are observed in the spectra at around 1660 cm^{-1} (C=O stretching vibrations of amide I), at about 1544 cm^{-1} (in plane N–H bending and C–N stretching vibrations of amide II), and 1610 cm^{-1} (the N–H stretching of amide).[22] The appearance of the peak at 1444 cm^{-1} is assigned to C=O vibration of carboxylic acids, [21] possibly originated form the free carboxyl groups of NH_2-BDC ligand or the hydrolysis of unreacted acyl-chloride groups.[22] Besides, the considerable increase of N–H bending vibrations at 1544 cm^{-1} can be ascribed to the NH_2-BDC ligand, which indicate the presence of Ag-MOFs nanorods.

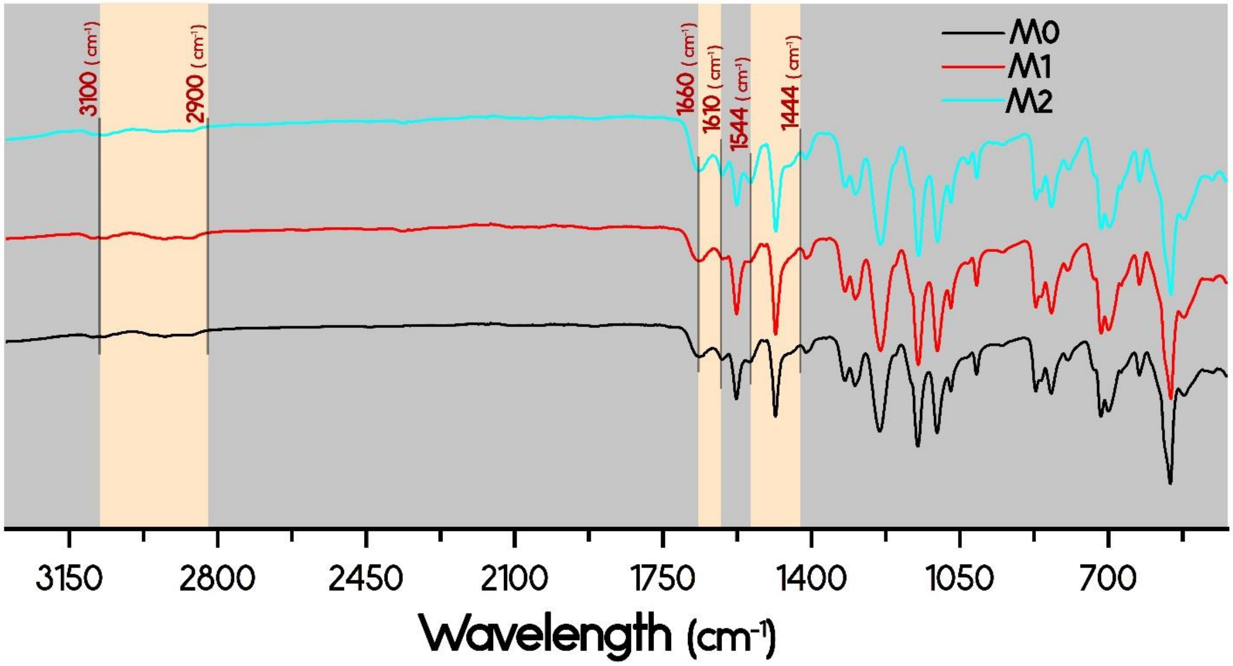

Figure 3. ATR-FTIR spectra of the neat M0, and the nanocomposite M1 and M2 membranes

Characteristics of the thin-film membranes. X-ray photoelectron spectroscopy (XPS) was performed to investigate the elemental composition and chemical bonds of the neat M0, and the M1 and M2 TFN membranes. As shown in **Figure 4**, the energy spectra of all membranes mainly included carbon (C), oxygen (O), and nitrogen (N) peaks, which were located at binding energies of 285 eV (assigned to C 1s), 400 eV (N 1s), and 531 eV (O 1s). [17, 33] The appearance of two new silver peaks observed at about 368 eV and 374 eV (corresponding to Ag $3d_{5/2}$ and $3d_{3/2}$, respectively) [34] suggests the presence of Ag-MOFs nanorods in the structure of TFN membranes. It must be noted that no silver signal was observed in the survey spectra of the neat M0 membrane (**Figure 4a**). Gaussian function was used for peak fitting. In high-resolution C 1s spectra (Figure 2b) three peaks can be identified: a major peak approximately at 285 eV [35], mostly attributed to the carbon atoms in benzene ring correlated to C−H, C−C, and C═C bonds; [36-37] an intermediate peak at 287 eV assigned to C−N, C−O, and C-O-C bonds; [38] and also a minor peak approximately at 288 eV attributed to O-C═O and amide O=C−N bonds. [17, 33, 37] High-resolution O 1s spectra are instead best fitted by two peaks: a major peak located at about 532.5 eV, assigned to C=O (N-C═O, O-C═O, and C═O bonds); and a minor peak around 533.5 eV related to C-O (O-C═O and C-O-H bonds). [17, 39-40]

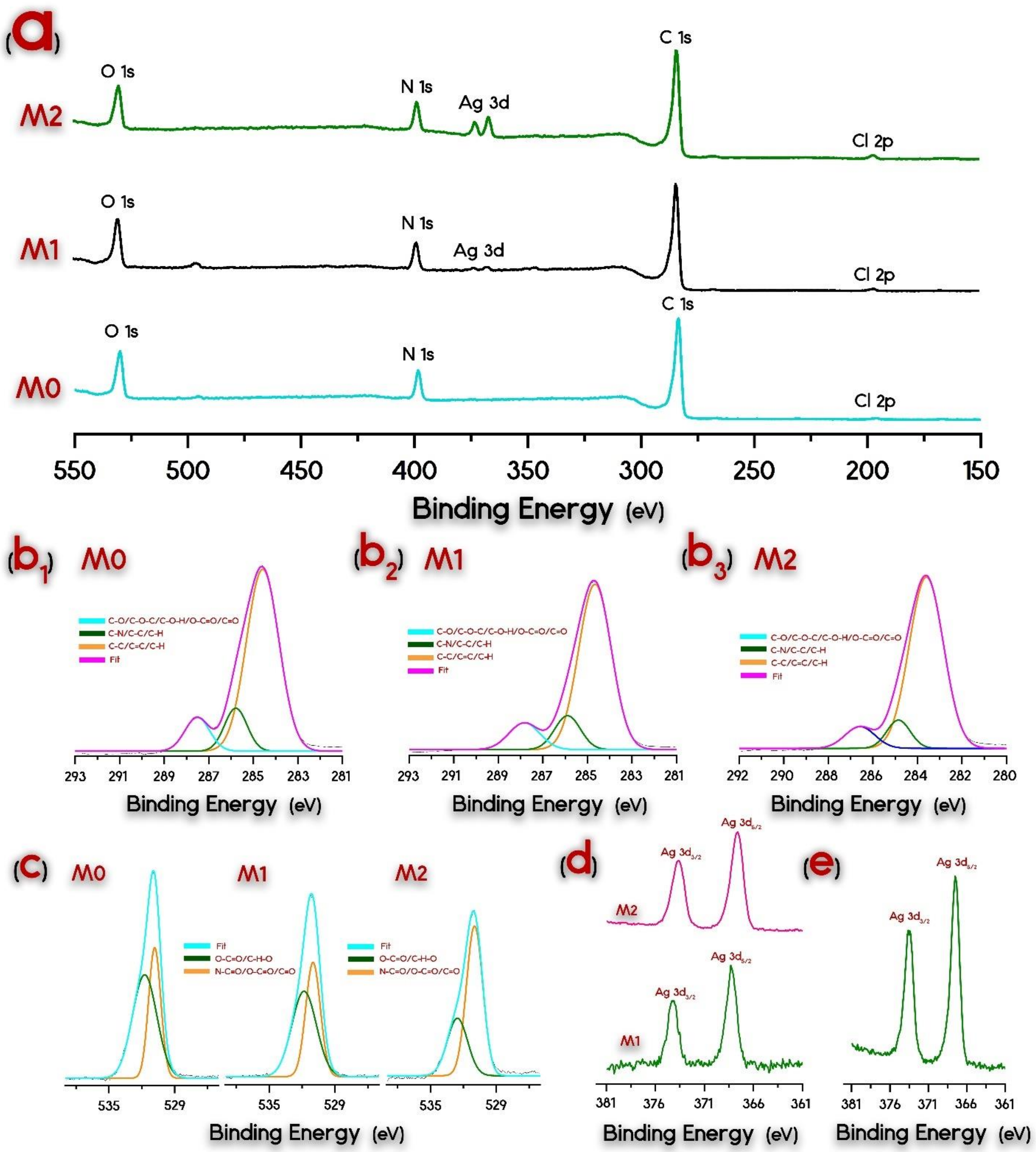

Figure 4. (a) XPS survey spectra of the neat M0, and of the M1 and M2 TFN membranes; de-convoluted high-resolution C (1s) spectra of (b_1) the neat M0, (b_2) M1 (b_3) and M2 TFN membranes; (c) de-convoluted high-resolution O (1s) spectra of the neat M0, and of the M1 and M2 TFN membranes; (d) de-convoluted high-resolution Ag spectra for M1 and M2 samples; and e) the intensity ratio,of Ag 3d spectra between M2 and M1 membranes.

The elemental compositions of all the membranes are reported in **Table 1**. Theoretically, the O/N ratio of polyamide varies between the value of 1 for a fully cross-linked structure to the value of 2 for a fully linear one. [41] A higher crosslinking degree reflects a denser polyamide structure with increased selectivity, while a lower degree offers improved hydrophilicity and higher permeability. The results of the elemental compositions (**Table 1**) indicate that the Ag-MOFs incorporation increased the O/N ratio for M1 and M2 TFN membranes, compared to that of the M0 membrane. This in turn can be interpreted as a lower degree of cross-linking of the polyamide structure.

On the other hand, what stands out in **Figure 4e** is that the intensity ratio of the XPS spectra related to silver for M2 and M1, $(\frac{\mathrm{M2}}{\mathrm{M1}})$, was about 6:1, indicating that the M2 sample contained more Ag on the outermost layer, despite the same amount of MOFs was added to the solutions during preparation. A likely explanation is that the IP reaction is primarily governed by the diffusion of MPD molecules into the reaction zone; therefore the polymer film grows from the interface toward the bulk of the organic solution, [31] thus entrapping more MOFs into the topmost polyamide layer (for M2 fabrication, nanorods were dispersed in the organic TMC solution). Considering that the penetration depth of the X-ray in XPS analysis is generally less than 10 nm of the top selective layer, [42] the results are rationalized with a higher concentration of Ag-MOFs near the topmost surface of M2 membranes, translating into a potentially higher content of Ag ions accessible to the surface. [43] **Figure 5** illustrates the relevant EDX mapping and EDX elemental composition of M1 (**Figure 5d**) and M2 (**Figure 5h**) nanocomposite membranes, clearly corroborating the presence of Ag atoms. It should be noted that the EDX analysis covers the entire thickness of sample, while XPS analysis covers roughly the uppermost portion of the selective layer. The Ag detected by EDX was almost identical for both M1 and M2 membranes. This result suggest that, while the same amount of Ag-MOFs was incorporated in the two membranes, the nanorods preferentially accumulated near the topmost surface of M2 membrane selective layers.

Table 1. Elemental compositions, O/N ratio, and Ag spectra intensity ratio of the membranes.

Membrane	Atomic concentration (%)				O/N ratio	M2/M1 Ag ratio (from spectra intensity)
	C (1s)	O (1s)	N (1s)	Ag (3d)		
M0	60.0	23.2	16.1	0.0	1.48	-
M1	59.7	25.7	12.5	2.0	2.05	-
M2	56.7	19.7	11.5	12.1	1.71	6.05

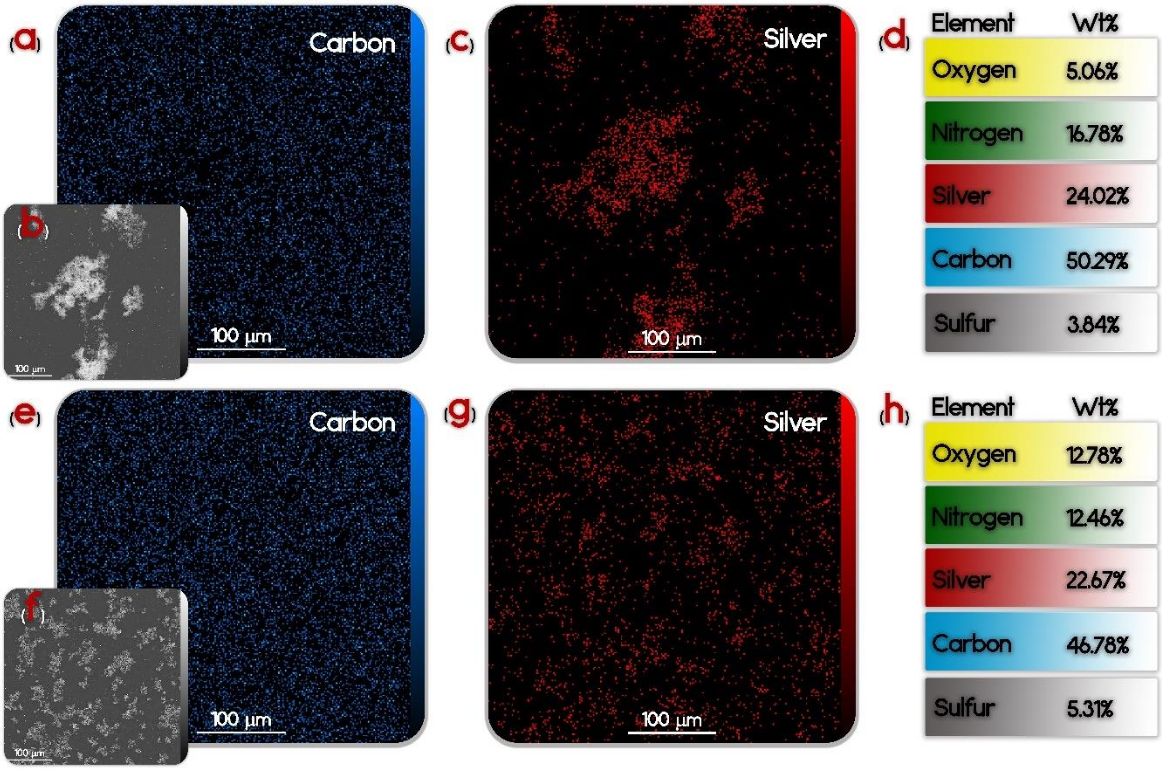

Figure 5. EDX analyses for a-d) M1 membrane and e-h) M2 membrane. a, e) EDX mapping of carbon; b, f) surface FESEM images; c, g) EDX mapping of silver; and d, h)EDX elemental compositions.

The surface and cross-section morphology of the membranes were analyzed by FESEM images, and some representative micrographs are presented in **Figure 6**. The neat M0 membrane (**Figures 6a**, and **6b**) exhibited a ridge-and-valley surface, which is the intrinsic morphology of polyamide membranes formed by the IP reaction. [44] Although no obvious change occurred in the top surface morphology of nanocomposite membranes, bright spots appeared on their surface upon the incorporation of Ag-MOFs nanorods in the layer. These features can be ascribed to the presence of Ag atoms within the core of Ag-MOFs nanorods. Such spots are more easily observed in the cross-sectional images, with a uniform distribution throughout the thickness of the M2 TFN sample (**Figure 6h**, and **6i**). Since the sensitivity of heavy elements, such as silver, to the backscatter electrons is significantly higher than that of light ones, such as carbon, nitrogen, and oxygen, [45] a backscattered imaging detector was applied to identify and isolate the heavy elements (see Figure S2, S3, S4). These small spots were uniformly distributed within the M1 and M2 TFN layers, whereas such bright spots were not detected while imaging the neat M0 membrane. These results may be interpreted with a high-density and rather homogenous dispersion of the Ag-MOFs nanorods within the polyamide layer of TFN membranes, corroborating the hypothesis that there is suitable compatibility between the two phases represented by nanorods and the polyamide matrix. [46] Moreover, the cross-sectional morphology of the M1 membrane shows that, by loading the aqueous MPD solution with Ag-MOFs during IP, the average thickness of the TFN layer decreased. [47] Indeed, the incorporation of the nanorods may thwart the MPD diffusion into the organic phase during polymerization and delay the formation of the polyamide film due to the steric hindrance of Ag-MOFs. [48] This decrement in layer thickness would diminish the mass transfer resistance and eventually result in improved water flux. [49]

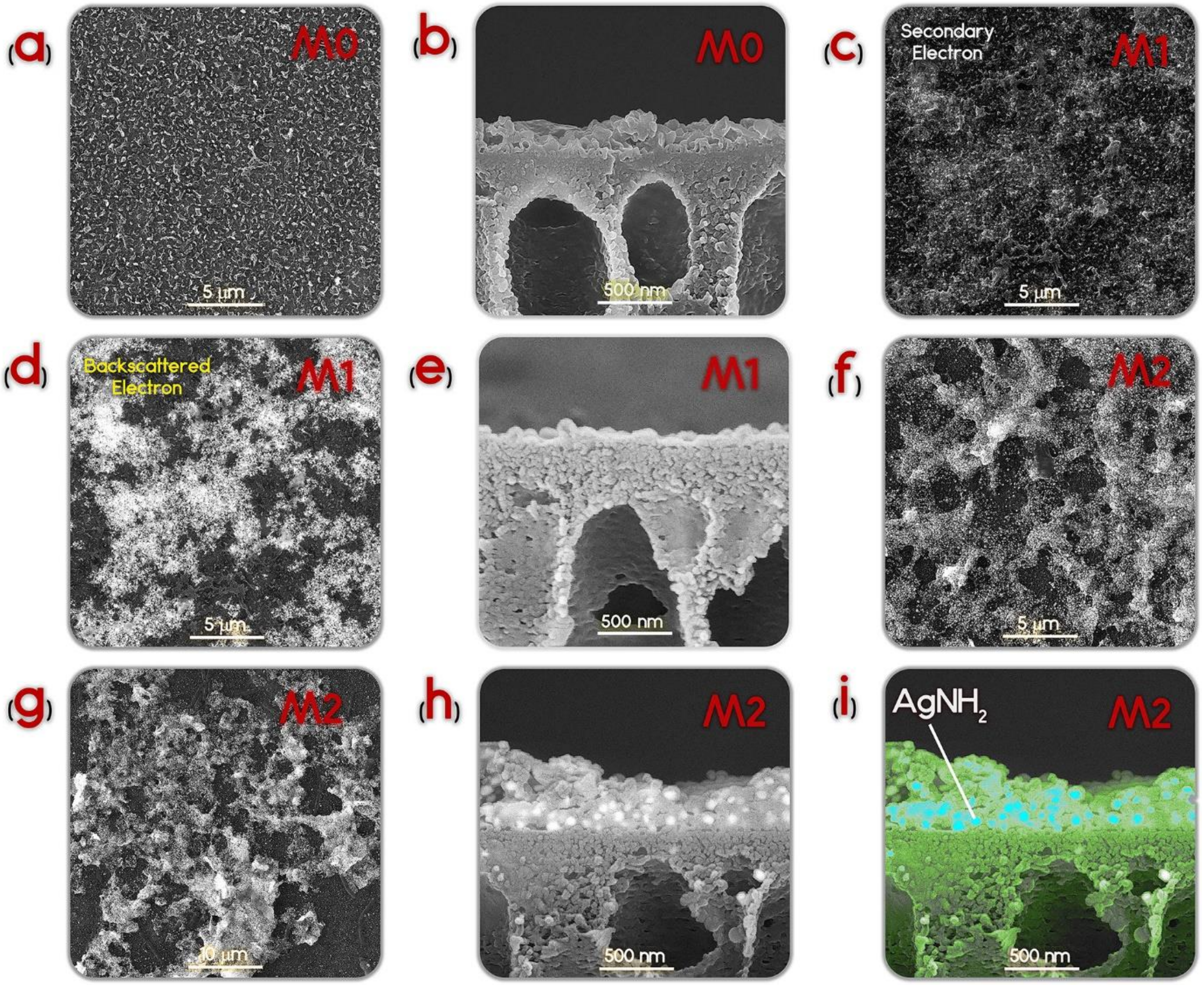

Figure 6. (a) Surface and (b) cross-sectional FESEM micrographs of the neat M0 membrane; (c) Surface in secondary mode, (d) Surface in backscatter mode and (e) cross-sectional FE-SEM micrographs of the M1 membrane; and (f and g) M2 membrane surface in backscatter mode, (i) cross-sectional and (i) colored cross-sectional SEM of the M2 membrane

More morphological features were observed using AFM, and the results are summarized in **Figure 7a** (roughness parameters) and **d_1-d_3** (three-dimensional AFM images, see Figure S5). The roughness parameters were higher for membranes fabricated by incorporation of Ag-MOFs nanorods, consistent with results from SEM observations, which suggested the formation of additional features within the polyamide due to the presence of Ag-containing nanorods. This result is especially true for M2 membranes, which showed significantly larger values of RMS and Rz roughness. This observation may again stem from the different fabrication procedure. During the preparation of M2, nanorods are dispersed in the TMC solution, and their amount near the organic/water interface is probably higher in comparison with the protocol to prepare M1 membrane, where only the pores of the support are soaked with the nanorod-containing MPD solution. Overall, from SEM, XPS, and AFM results, it can be concluded that dispersing nanomaterials in the organic solution (M2 membrane) results in a thicker and rougher selective film, with a higher density of Ag-MOF nanorods embedded in the topmost portion of this layer. It has been reported that rougher membranes are generally more prone to biofouling by bacterial cells and macromolecules. However, a complex relationship exists between roughness, hydrophilicity, and fouling behavior, which cannot be solely rationalized from the surface morphological analysis. [50]

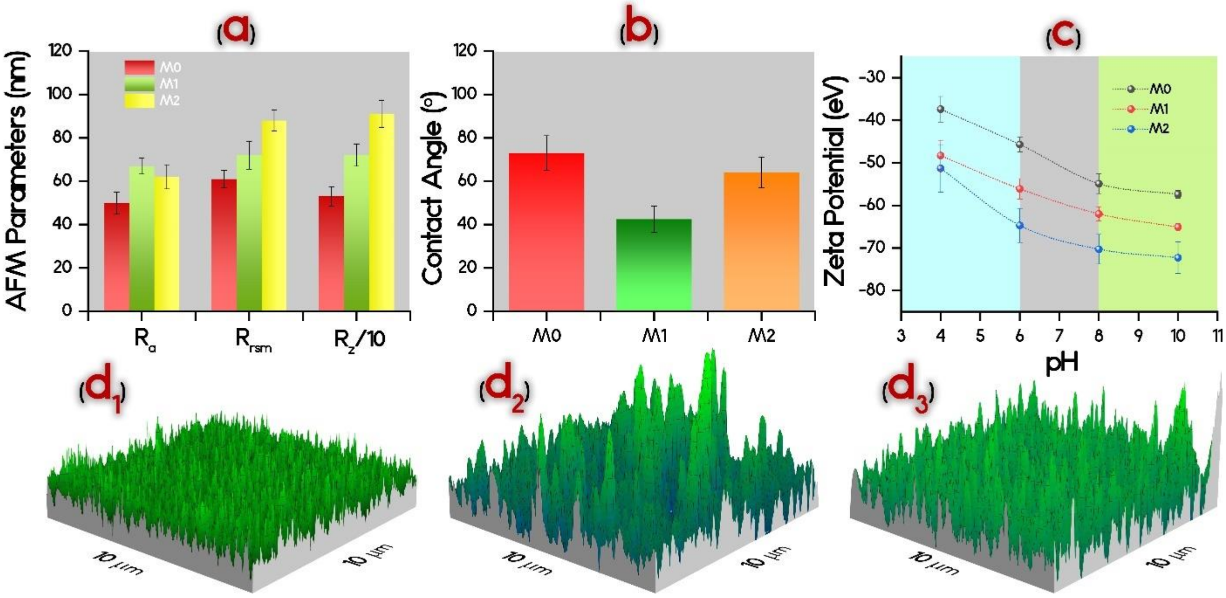

Figure 7. a) AFM roughness parameters; b) contact angles; c) zeta potential; and representative AFM images of (d_1) M0, (d_2) M1, and (d_3) M2 membranes.

To obtain information on the surface hydrophilicity, the average water contact angle of the membranes was measured and the results are presented in **Figure 7b**. The average contact angle reduced from 72.6±5.1 degrees for the neat M0 membrane to 43.4±3.1 and 63.2±2.8 degrees for M1 and M2 samples, respectively. This increment in the membrane wettability probably originates from the presence of hydrophilic Ag-MOFs nanorods, which contain numerous functional groups on their surface that have a tendency to form hydrogen bonds with water molecules. Although larger roughness was observed for the nanocomposite membranes, the role of surface chemistry often offsets that of surface roughness in the rate of fouling during membrane filtration. [50] The likelihood of hydrogen bonding between the membrane surface and the surrounding water molecules promotes the formation of a thin layer of water at the surface/liquid interface, which prevents bacteria deposition and alleviates the undesirable attachment of hydrophobic foulants in general. [51]

The surface charge is also a crucial factor when it comes to treating a feed solution with charged foulants. [52-53] A negatively-charged membrane is typically less prone to biofouling by bacterial cells, which carry a net negative charge in the pH range 4–9, through electrostatic repulsion. [54] **Figure 7c** reports the results of zeta potential for the membranes as a function of pH. The results are in agreement with the protonation behavior of polyamide carboxyl groups deprotonating at increased pH values, thus imparting an overall negative potential to the surface. [55] What is interesting in the data presented in **Figure 7c** is the larger values of negative zeta potential of both M1 and M2 nanocomposite membranes compared to traditional polyamide membranes. This result may be attributed to the additional contribution of the free carboxylic groups present in the framework of Ag-MOFs nanorods. M2 membranes showed the largest negative charge among the membranes, which may again be attributed to the higher density of

Ag-MOFs nanorods at the surface. This increased negative surface potential of both nanocomposite membranes may eventually result in reduced biofouling. [56]

Membrane Transport Properties. The transport parameters of the membranes were determined based on a four-step FO procedure, [57] and the results are listed in **Table 2** and **Figure 8**. The results in terms of water flux, reverse salt flux, and water to reverse salt flux ratio are presented in Figure 8. The results indicate that J_w of M1 membrane was higher while that of M2 membrane was lower than the water flux observed for the pristine M0 membrane. Furthermore, J_s of both M1 and M2 membranes was considerably smaller in comparison to M0 membranes. Overall, the specific solute flux (J_s/J_w) is a key membrane performance parameter, which should be low to allow high selectivity in the FO process. As presented in Figure 8.c, both M1 and M2 TFN membranes showed lower J_s/J_w ratio (higher (J_w/J_s)) compared to M0. Nonetheless, this difference was less marked for M2 due to a lower value of water flux obtained with this membrane, which can be rationalized with the increased thickness of its selective layer, as suggested by FESEM micrographs.

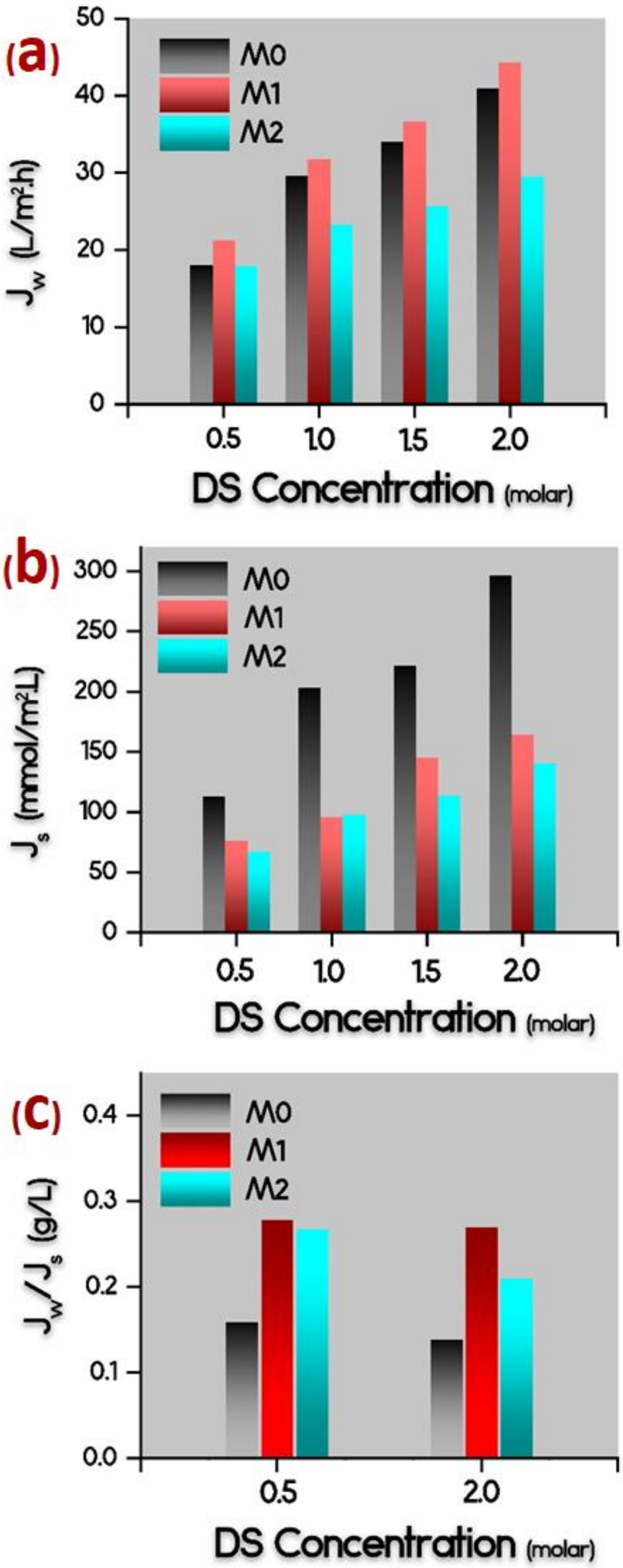

Figure 8. (a) The water flux, (b) Solute flux, (c) water over solute flux fraction versus the molar concentration of the NaCl draw solution.

From the data shown in Figure 8, the intrinsic transport properties of the polyamide or nanocomposite polyamide layers can be calculated (Table 2). Surprisingly, the water permeability coefficient, *A*, increased from 1.1 to 2.24 L $m^{-2}h^{-1}bar^{-1}$ while the *B* value increased only slightly, from 0.33 to 0.41 L $m^{-2}h^{-1}$ when nanorods were incorporated into the layer to form M1 membranes. The same trend but of lower magnitude was observed for the M2 membranes. Therefore, the ratio of solute permeability/water permeability (*B/A* ratio) decreased when membranes were synthesized by incorporating Ag-MOFs within the polyamide layer, suggesting the enhanced performance of the nanocomposite membranes. The lower the *B/A* ratio, the more enhanced the selectivity and the sustainability of the FO process. [58-59] The improved transport properties may be related to the increased hydrophilicity compared to conventional polyamide membrane. Another reason for the enhanced permeation properties of nanocomposite membranes can be the formation of nano-sized voids at the interface of MOFs and polyamide matrix. Normally, inhomogeneous distribution of NPs in the top polyamide layer due to their aggregation and their weak compatibility with the polymer are two limiting factors that negatively affect the performance of the TFN membrane. [60] Since the thickness of the polyamide selective layer falls in the range of 100-300 nm, nanomaterials must have a significantly smaller size of at most tens of nanometers to prevent defect formation, which would translate into compromised salt selectivity. In the present work, although Ag-MOFs nanorods offered improved compatibility with the polyamide matrix, some gaps may still form between polymeric chains during the IP reaction. These gaps would increase the void fractional volume and provide more facile transport of both water and salt molecules. However, in this study, the effect of these voids on the transport of water seemed overwhelming compared to that on salt, leading to enhanced overall performance. [61]

Table 2. Transport Properties of the Membranes.

Membrane	A	B	B/A	S	R^2 (J_w)	R^2 (J_s)
M0	1.10±0.1	0.335±0.02	0.34±0.01	123±1	0.98±0.02	0.95±0.1
M1	2.24±0.1	0.410±0.02	0.293±0.01	206±1	0.975±0.01	0.879±0.1
M2	1.49±0.1	0.366±0.02	0.245±0.01	279±1	0.907±0.01	0.924±0.1

A: water permeability coefficient (L $m^{-2}h^{-1}bar^{-1}$)
B: solute permeability coefficient (L $m^{-2}h^{-1}$)
R^2 (J_w): water flux coefficient of determination
R^2 (J_s): solute flux coefficient of determination

Antibacterial Properties of the Membranes. The antibacterial properties of the membranes were first evaluated by live and dead staining and observed by fluorescence microscopy. **Figure 9a_1-a_3** reports representative fluorescent images of the bacteria attached to the membranes after incubation in the bacterial suspension. Nearly all bacteria on the conventional TFC membrane surface were alive following incubation; in contrast, the number of viable bacteria remaining on the surface of TFN membranes was reduced substantially. Mortality rates of approximately 90% and 96% were observed following incubation with the M1 and M2 TFN membranes, respectively. Notably, these high bacterial inactivation rates were obtained by loading a low concentration of the nanorods (0.2% by mass). [62] The disc inhibition zone method also illustrated that contact with the membrane surface inhibited biofilm growth on the plate (**Figure 9c_1-c_3**). Specifically, no inhibition zone for M0 membrane was observed, while there was a clear inhibition zone for both M1 and M2 membranes.

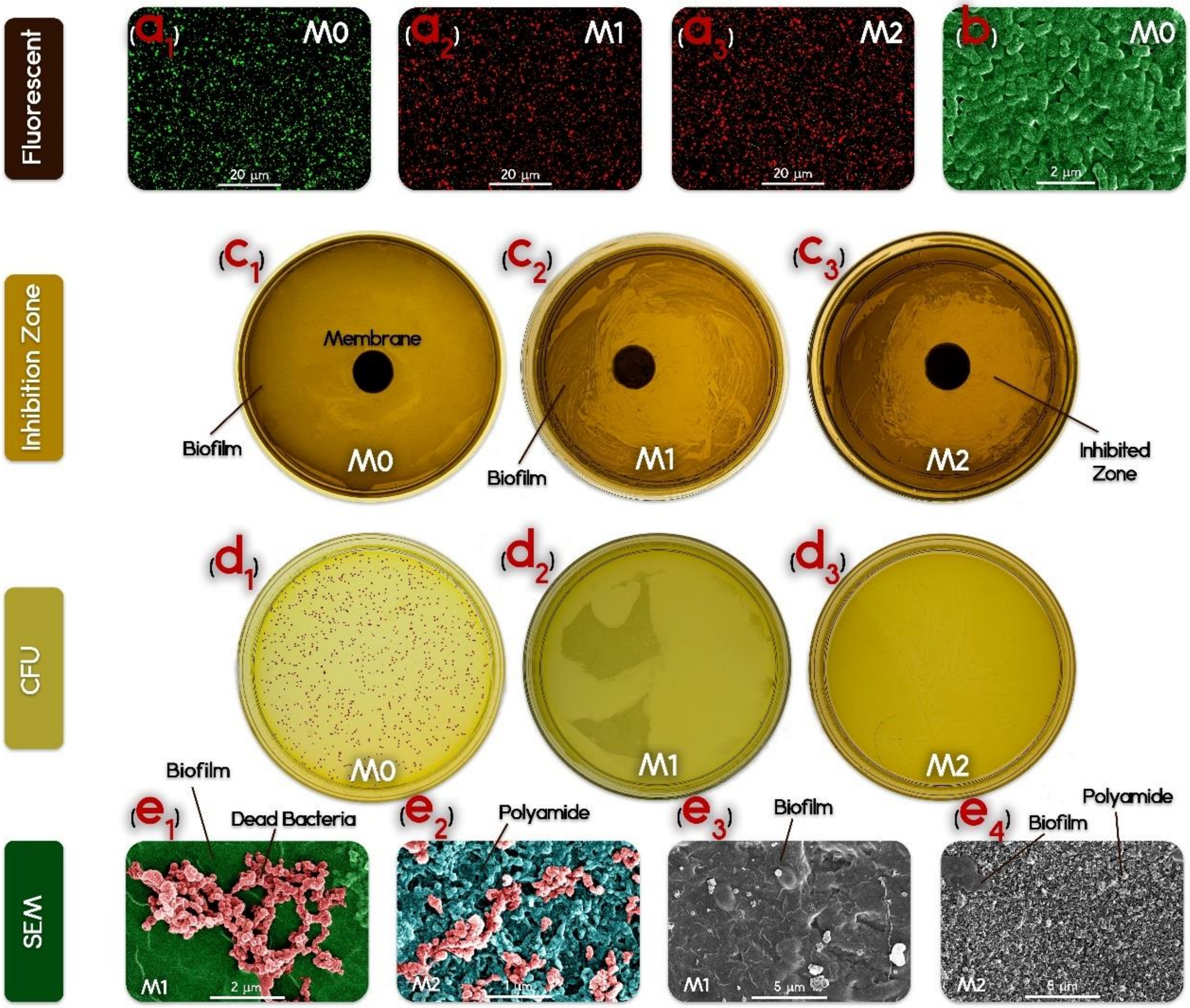

Figure 9. Antibacterial properties of the membranes. Fluorescent images of *E. coli* cells attached to the surface of a_1-a_3) neat M0, M1, and M2 membranes, respectively; stained by SYTO 9 (green) and PI (red) for live and dead cells, respectively; b) SEM images of live bacteria attached to the surface of M0 membrane; disc inhibition zone test results obtained with c_1-c_3) neat M0, M1, and M2 membranes, respectively; colony-forming units from plating bacterial suspension previously in contact with d_1-d_3) neat M0, M1, and M2 membranes, respectively; e_1-e_4) SEM images of the bacterial cells attached to the surface M1 and M2 membranes.

The colony-forming unit experiments (**Figure 9d_1-d_3**), in which unattached cells were plated after the biological suspensions were placed in contact with the membrane, also suggested a strong biocidal effect for both M1 and M2 membranes. Almost no viable cells were visible after contact with M1 and M2, as opposed to M0, on which many marked colonies formed instead. Finally, SEM images (**Figure 9b** and **9e$_1$-e$_4$)** showed healthy *E. coli* cells (**Figure 9b**) on M0 membrane and degraded *E. coli* cells on M1 (**Figure 9e$_1$** and**e$_3$**) and M2 membranes (**Figure 9e$_2$** and **e$_4$**), consistent with the results discussed above. Taking a closer look at SEM images, a uniform biofilm is visible on M1 but consisting of bacteria whose structure was clearly compromised, while little biofilm was formed on M2 membranes.

The results summarized in Figure 9 suggest high antibacterial activity of the nanocomposite membranes against gram-negative bacteria. The high inactivation rate observed in this study was attained after a short period of contact between the bacteria and the membrane (one hour); generally, a longer incubation time (greater than two hours) has been reported to obtain such behavior. [63] This observation indicates that, despite being mostly buried within a polyamide layer, Ag-MOFs nanorods are still active and can trigger bacterial inactivation at the membrane surface. MOFs can act as Ag^+ ions reservoir in which the gradual release of the metal center to the surrounding environment is the most probable cause for the toxicity of MOFs. [14, 64-6667] The content of antibacterial cations in Ag-MOFs is relatively high. [65-66, 68] The Ag active sites in the structure of Ag-MOFs nanorods are uniformly distributed, and the release mechanism of Ag ions should not change during the degradation of the framework. Since the antibacterial activity is directly related to the release of Ag^+ ions, [66] the greater the quantity of released ions, the higher the inactivation rates. The concurrent gradual release of the organic linker present in the MOFs structure may result in a synergetic antimicrobial property. [15, 6469] While the most probable antibacterial mechanism is related to release of Ag^+, other possible antibacterial mechanisms proposed for Ag-MOFs biocidal activity are: (i) direct attachment to bacterial cells, infiltration and physical destruction of the cell membrane, and (ii) indirect generation of reactive oxygen species which trigger damage to the bacteria cell structure. [70] Overall, it is desirable to locate the

Ag-containing nanomaterials as much as possible near the membrane surface, where maximum interaction and direct exposure to the bacteria can be attained. In this study, Ag-MOFs nanorods with small size were homogenously distributed within the TFN membrane active layer and this resulted in successful inhibition of biofilm formation. The Ag-MOFs nanorods were immobilized with higher density near the surface of the nanocomposite layer of M2 membrane (as discussed in Figs 5 and 6). This configuration may be responsible to the higher antibacterial activity of M2.

Dynamic Organic Fouling and Biofouling Evaluation. The evaluation of flux decline in FO filtration due to organic fouling was performed using sodium alginate (SA) as representative organic foulant, and the results are provided in **Figure 10a**. Prior to each fouling or biofouling experiment, a baseline experiment was performed to eliminate the effect of draw solution dilution and reverse solute diffusion. The nanocomposite membranes demonstrated both reduced flux decline and higher flux recovery ratio compared to M0 samples. This antifouling property can be ascribed to the more hydrophilic nature of the surface of Ag-MOFs-incorporated TFN membranes. [71] To investigate the effect of Ag-MOFs nanorods on biofouling, filtrations were instead conducted using a synthetic wastewater feed containing *E. coli*. The results from biofouling experiments are presented in **Figure 10b**. Also in this case, the performance of the nanocomposite membrane was remarkably better than that of conventional membrane in terms of both reduced flux decline and improved flux recovery ratio. In this case, the improvement in performance can be attributed both to higher hydrophilicity, translating into lower bacterial deposition probability, and to the significant antibacterial activity of Ag-MOFs nanorods, which prevented biofilm proliferation. Although the M2 membrane provided higher antibacterial activity, the M1 was characterized by higher hydrophilicity and a smoother surface, thus reducing the total surface area accessible to bacterial cell accumulation and possibly leading to lower biofouling tendency and higher flux recovery ratio.

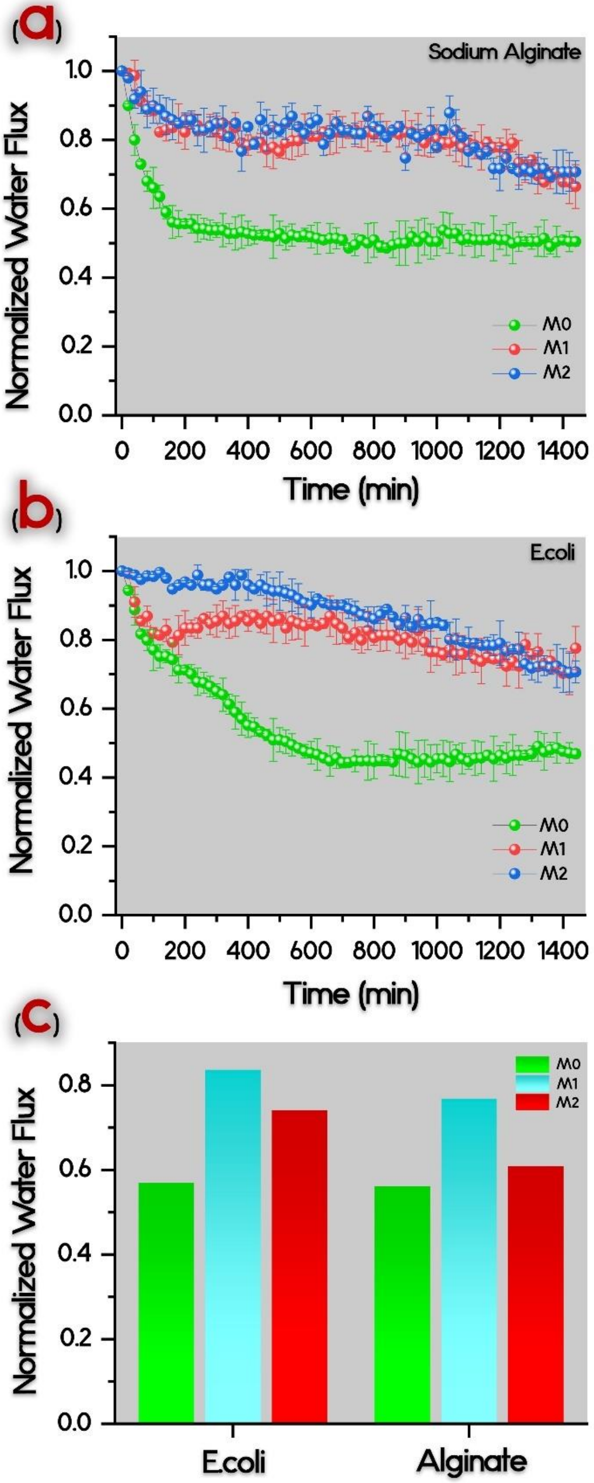

Figure 10. Results of fouling experiments under FO filtration conditions, using 1 M NaCl as DS: (a) organic fouling by alginate; (b) microbial fouling by *E. coli* (the standard deviation of three runs with fresh membrane samples); and c) the relevant water flux recovery ratios.

Stability and Release of Silver Ions. The robustness of the antibacterial and anti-biofouling activity of the functionalized membranes depends strongly on the controlled release of silver. [15] The MOF nanorods act as reservoirs of silver, which slowly leaks out into solution at the interface between the membrane and the feed solution or at the zone of biofilm attachment on the membrane surface. Therefore, the silver release rate was evaluated using ICP-MS for 15 days for the nanocomposite membranes. The two membranes showed the same initial trend of increase in silver release rate in the first 7 days of monitoring (see Figure 11, showing the cumulative trend of Ag ions leakage), whereby the release rate in the 7 first days was more significant than in the following 8 days. The M1 sample showed a lower overall release rate compared to the M2 sample. This difference most probably stems from the much more concentrated presence of Ag-MOFs close to the membrane surface for the M2 sample, as discussed abpve. Nevertheless, the overall release rate of silver ion for both membranes was low and finally reached values of 0.3 and 0.2 µmol/L for the M1 and M2 membranes (below standard concentration of 0.1 mg/L), respectively. [8, 17]

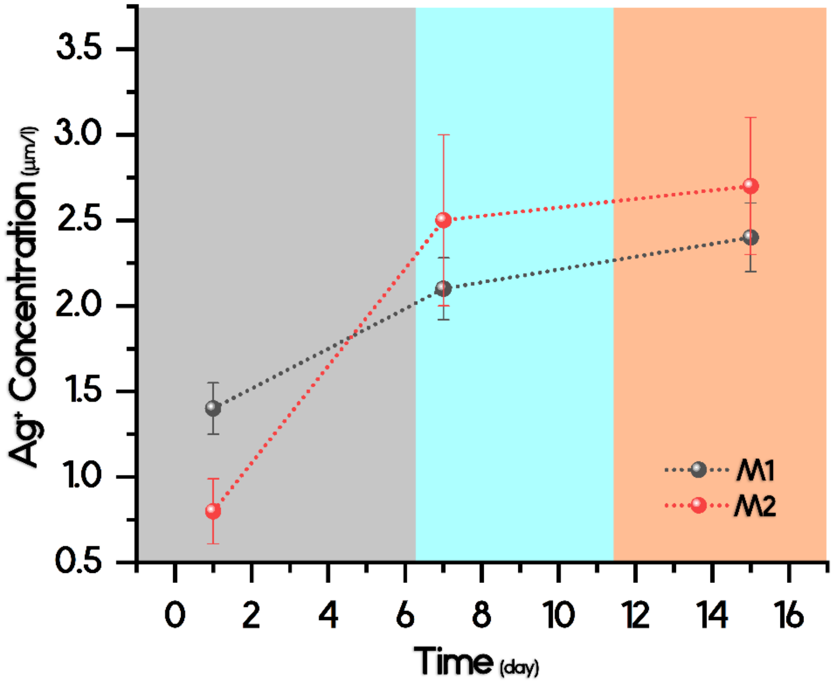

Figure 11. Silver ion leaching from the nanocomposite membranes.

CONCLUSION

In this work, Ag-MOFs nanorods were successfully synthesized and then embedded within the polyamide matrix of forward osmosis membranes to improve their antifouling and antibacterial properties. We fabricated novel Ag-MOFs nanorods comprising amine functional groups, which interacted favorably with monomers during polyamide formation, as well as with polyamide chains themselves. This mechanism ensured the compatibility of Ag-MOFs nanorods with the surrounding matrix and allowed suitable dispersion within the polyamide film without an adverse impact on the integrity of the selective layer. Two approaches were employed for the preparation of nanocomposite membranes, one entailing the dispersion of the nanorods in the aqueous solution during interfacial polymerization, the other involving dispersion in the organic solution. In both cases, the results of membrane characterizations demonstrated the presence of

Ag-MOFs nanorods in the polyamide layer. The incorporation of Ag-MOFs nanorods increased surface hydrophilicity and improved the performance of the membranes in forward osmosis. In addition, the nanocomposite membranes presented an excellent antifouling performance for both organic and biological foulants, presenting 84% and 73% flux recovery ratio following fouling and simple physical cleaning of the membrane. This effect was partly attributed to the observed antibacterial effect of Ag-MOFs nanorods. The suitable incorporation of Ag-MOFs nanorods within the polyamide matrix was also corroborated by slow leaching of silver in aqueous solution, suggesting the potential to impart prolonged activity during operation.

When comparing the two fabrication approaches, the results suggested that dispersing the nanorods in the organic TMC phase during fabrication produced a thicker and rougher membrane, with a large density of Ag-MOFs embedded in the uppermost portion of the membrane selective layer. In contrast, dispersing the MOFs in the aqueous MPD solution likely slowed the diffusion of this monomer into the organic phase during IP, translating into a thinner and smoother selective layer incorporating nanorods in a more homogeneous fashion throughout the membrane cross-section. Ultimately, directly due to these phenomena, the M2 TFN membrane showed higher antibacterial activity, while the M1 presented overall better filtration performance and lower fouling-related flux declines owing to its properties comprising of both suitable antibacterial properties and better hydrophilicity and surface smoothness.

Supporting Information

Further detailed information on materials and methods (SI.1):, evaluation of the membrane transport properties (SI.1.1.), dynamic fouling experiments (SI.1.2.), fluorescent scanning microscopy (SI.1.3.), and quantifying quantification of the release of silver ions from the membrane (SI.1.4.); The dDigital images of the MPD aqueous and TMC organic solutions immediately after the addition of Ag-MOFs nanorods (Figure S1); FESEM images of the M1 membrane at different magnifications in secondary and backscatter modes (Figure S2); Surface FE-SEM images of the M2 membrane at different magnifications in secondary and backscatter modes (Figure S3); High magnification FESEM images of the M1 and M2 membranes in secondary and backscatter modes (Figure S4); AFM images of the neat M0, M1, and M2 membranes (Figure S5).″.

References

(1) Saqib, J.; Aljundi, I. H. Membrane fouling and modification using surface treatment and layer-by-layer assembly of polyelectrolytes: state-of-the-art review. *Journal of Water Process Engineering* **2016,** *11*, 68-87.

(2) Esfahani, M. R.; Aktij, S. A.; Dabaghian, Z.; Firouzjaei, M. D.; Rahimpour, A.; Eke, J.; Escobar, I. C.; Abolhassani, M.; Greenlee, L. F.; Esfahani, A. R. J. S.; Technology, P. Nanocomposite membranes for water separation and purification: Fabrication, modification, and applications. **2019,** *213*, 465-499.

(3) Kebria, M. R. S.; Rahimpour, A.; Salestan, S. K.; Seyedpour, S. F.; Jafari, A.; Banisheykholeslami, F.; Kiadeh, N. T. H. Hyper-branched dendritic structure modified PVDF electrospun membranes for air gap membrane distillation. *Desalination* **2020,** *479*, 114307.

(4) Firouzjaei, M. D.; Seyedpour, S. F.; Aktij, S. A.; Giagnorio, M.; Bazrafshan, N.; Mollahosseini, A.; Samadi, F.; Ahmadalipour, S.; Firouzjaei, F. D.; Esfahani, M. R. J. J. o. M. S. Recent advances in functionalized polymer membranes for biofouling control and mitigation in forward osmosis. **2019**, 117604.

(5) Mozafari, M.; Seyedpour, S. F.; Salestan, S. K.; Rahimpour, A.; Shamsabadi, A. A.; Firouzjaei, M. D.; Esfahani, M. R.; Tiraferri, A.; Mohsenian, H.; Sangermano, M. Facile Cu-BTC surface modification of thin chitosan film coated polyethersulfone membranes with improved antifouling properties for sustainable removal of manganese. *Journal of Membrane Science* **2019**, 117200.

(6) Esfahani, M. R.; Koutahzadeh, N.; Esfahani, A. R.; Firouzjaei, M. D.; Anderson, B.; Peck, L. J. J. o. m. s. A novel gold nanocomposite membrane with enhanced permeation, rejection and self-cleaning ability. **2019,** *573*, 309-319.

(7) Hermans, S.; Mariën, H.; Van Goethem, C.; Vankelecom, I. F. Recent developments in thin film (nano) composite membranes for solvent resistant nanofiltration. *Current Opinion in Chemical Engineering* **2015,** *8*, 45-54.

(8) Rahimpour, A.; Seyedpour, S. F.; Aghapour Aktij, S.; Dadashi Firouzjaei, M.; Zirehpour, A.; Arabi Shamsabadi, A.; Khoshhal Salestan, S.; Jabbari, M.; Soroush, M. Simultaneous Improvement of Antimicrobial, Antifouling, and Transport Properties of Forward Osmosis Membranes with Immobilized Highly-Compatible Polyrhodanine Nanoparticles. *Environ. Sci. Technol.* **2018**.

(9) Kim, I.-C.; Jeong, B.-R.; Kim, S.-J.; Lee, K.-H. Preparation of high flux thin film composite polyamide membrane: the effect of alkyl phosphate additives during interfacial polymerization. *Desalination* **2013,** *308*, 111-114.

(10) Mollahosseini, A.; Rahimpour, A. A new concept in polymeric thin-film composite nanofiltration membranes with antibacterial properties. *Biofouling* **2013,** *29* (5), 537-548.

(11) Tang, C.; Li, X.; Li, Z.; Hao, J. Interfacial Hydrogen Bonds and Their Influence Mechanism on Increasing the Thermal Stability of Nano-SiO2-Modified Meta-Aramid Fibres. *Polymers* **2017,** *9* (10), 504.

(12) Seyedpour, S. F.; Rahimpour, A.; Esfahani, M. R., Methods of making nanostructured metal-organic frameworks. Google Patents: 2020.

(13) Firouzjaei, M. D.; Afkhami, F. A.; Esfahani, M. R.; Turner, C. H.; Nejati, S. J. J. o. W. P. E. Experimental and molecular dynamics study on dye removal from water by a graphene oxide-copper-metal organic framework nanocomposite. **2020,** *34*, 101180.

(14) Seyedpour, S. F.; Rahimpour, A.; Najafpour, G. Facile in-situ assembly of silver-based MOFs to surface functionalization of TFC membrane: A novel approach toward long-lasting biofouling mitigation. *Journal of Membrane Science* **2019,** *573*, 257-269.

(15) Wyszogrodzka, G.; Marszałek, B.; Gil, B.; Dorożyński, P. Metal-organic frameworks: mechanisms of antibacterial action and potential applications. *Drug discovery today* **2016,** *21* (6), 1009-1018.

(16) Li, J.; Wang, H.; Yuan, X.; Zhang, J.; Chew, J. W. Metal-organic framework membranes for wastewater treatment and water regeneration. *Coordination Chemistry Reviews* **2020,** *404*, 213116.

(17) Firouzjaei, M. D.; Shamsabadi, A. A.; Aktij, S. A.; Seyedpour, S. F.; Sharifian Gh, M.; Rahimpour, A.; Esfahani, M. R.; Ulbricht, M.; Soroush, M. Exploiting Synergetic Effects of Graphene Oxide and a Silver-Based Metal–Organic Framework To Enhance Antifouling and Anti-Biofouling Properties of Thin-Film Nanocomposite Membranes. *ACS applied materials & interfaces* **2018,** *10* (49), 42967-42978.

(18) Tiraferri, A.; Kang, Y.; Giannelis, E. P.; Elimelech, M. Superhydrophilic thin-film composite forward osmosis membranes for organic fouling control: fouling behavior and antifouling mechanisms. *Environ. Sci. Technol.* **2012,** *46* (20), 11135-11144.

(19) Seyedpour, S. F.; Rahimpour, A.; Shamsabadi, A. A.; Soroush, M. Improved performance and antifouling properties of thin-film composite polyamide membranes modified with nano-sized bactericidal graphene quantum dots for forward osmosis. *Chemical Engineering Research and Design* **2018,** *139*, 321-334.

(20) Yi, M.; Lau, C. H.; Xiong, S.; Wei, W.; Liao, R.; Shen, L.; Lu, A.; Wang, Y. J. A. a. m.; interfaces. Zwitterion–Ag Complexes That Simultaneously Enhance Biofouling Resistance and Silver Binding Capability of Thin Film Composite Membranes. **2019,** *11* (17), 15698-15708.

(21) Yin, J.; Zhu, G.; Deng, B. Graphene oxide (GO) enhanced polyamide (PA) thin-film nanocomposite (TFN) membrane for water purification. *Desalination* **2016,** *379*, 93-101.

(22) Baig, M. I.; Ingole, P. G.; Choi, W. K.; Jeon, J.-d.; Jang, B.; Moon, J. H.; Lee, H. K. Synthesis and characterization of thin film nanocomposite membranes incorporated with surface functionalized Silicon nanoparticles for improved water vapor permeation performance. *Chem. Eng. J.* **2017,** *308*, 27-39.

(23) Wei, X.; Wang, Z.; Wang, J.; Wang, S. A novel method of surface modification to polysulfone ultrafiltration membrane by preadsorption of citric acid or sodium bisulfite. *Membrane Water Treatment* **2012,** *3* (1), 35-49.

(24) Wu, Z.; Li, S.; Liu, M.; Wang, Z.; Liu, X. Liquid oxygen compatible epoxy resin: modification and characterization. *RSC Advances* **2015,** *5* (15), 11325-11333.

(25) Firouzjaei, M. D.; Shamsabadi, A. A.; Sharifian Gh, M.; Rahimpour, A.; Soroush, M. A novel nanocomposite with superior antibacterial activity: a silver-based metal organic framework embellished with graphene oxide. *Advanced Materials Interfaces* **2018,** *5* (11), 1701365.

(26) Waterhouse, G. I.; Bowmaker, G. A.; Metson, J. B. The thermal decomposition of silver (I, III) oxide: A combined XRD, FT-IR and Raman spectroscopic study. *Physical Chemistry Chemical Physics* **2001,** *3* (17), 3838-3845.

(27) Perera, D. H. N.; Song, Q.; Qiblawey, H.; Sivaniah, E. Regulating the aqueous phase monomer balance for flux improvement in polyamide thin film composite membranes. *Journal of membrane science* **2015,** *487*, 74-82.

(28) Ali, M. E.; Wang, L.; Wang, X.; Feng, X. Thin film composite membranes embedded with graphene oxide for water desalination. *Desalination* **2016,** *386*, 67-76.

(29) Bano, S.; Mahmood, A.; Kim, S.-J.; Lee, K.-H. Graphene oxide modified polyamide nanofiltration membrane with improved flux and antifouling properties. *Journal of Materials Chemistry A* **2015,** *3* (5), 2065-2071.

(30) Saha, N.; Joshi, S. Performance evaluation of thin film composite polyamide nanofiltration membrane with variation in monomer type. *Journal of Membrane Science* **2009,** *342* (1-2), 60-69.

(31) Khorshidi, B.; Thundat, T.; Fleck, B.; Sadrzadeh, M. J. R. A. Thin film composite polyamide membranes: parametric study on the influence of synthesis conditions. **2015,** *5* (68), 54985-54997.

(32) Wei, X.; Wang, Z.; Wang, J.; Wang, S. A novel method of surface modification to polysulfone ultrafiltration membrane by preadsorption of citric acid or sodium bisulfite. *Memb. Water Treat* **2012,** *3*, 35-49.

(33) Liu, R.; Xian, Z.; Zhang, S.; Chen, C.; Yang, Z.; Li, H.; Zheng, W.; Zhang, G.; Cao, H. Electrochemical-reduction-assisted assembly of ternary Ag nanoparticles/polyoxometalate/graphene nanohybrids and their activity in the electrocatalysis of oxygen reduction. *Rsc Advances* **2015,** *5* (91), 74447-74456.

(34) Park, S.-H.; Kim, S. H.; Park, S.-J.; Ryoo, S.; Woo, K.; Lee, J. S.; Kim, T.-S.; Park, H.-D.; Park, H.; Park, Y.-I. Direct incorporation of silver nanoparticles onto thin-film composite membranes via arc plasma deposition for enhanced antibacterial and permeation performance. *J Memb Sci.* **2016,** *513*, 226-235.
(35) Khorshidi, B.; Thundat, T.; Fleck, B. A.; Sadrzadeh, M. J. S. r. A novel approach toward fabrication of high performance thin film composite polyamide membranes. **2016,** *6*, 22069.
(36) Liu, Z.; Ou, J.; Wang, H.; You, X.; Ye, M. Synthesis and characterization of hydrazide-linked and amide-linked organic polymers. *ACS applied materials & interfaces* **2016,** *8* (46), 32060-32067.
(37) Wagner, C.; Naumkin, A.; Kraut-Vass, A.; Allison, J.; Powell, C.; Rumble Jr, J. NIST X-ray Photoelectron Spectroscopy Database, NIST Standard Reference Database 20, Version 3.4 (Web Version). *U. S. Department of Commerce.* **2003**.
(38) Sun, Y.; Hu, J.; An, S.; Zhang, Q.; Guo, Y.; Song, D.; Shang, Q. Selective esterification of glycerol with acetic acid or lauric acid over rod-like carbon-based sulfonic acid functionalized ionic liquids. *Fuel* **2017,** *207*, 136-145.
(39) Kim, S.; Yun, Y.-S.; Choi, Y.-E. Development of waste biomass based sorbent for removal of cyanotoxin microcystin-LR from aqueous phases. *Bioresource technology* **2018,** *247*, 690-696.
(40) Beamson, G. High resolution XPS of organic polymers. *The Scienta ESCA 300 Database* **1992**.
(41) Benavente, J.; Vázquez, M. Effect of age and chemical treatments on characteristic parameters for active and porous sublayers of polymeric composite membranes. *J. Colloid Interface Sci.* **2004,** *273* (2), 547-555.
(42) Ariza, M.; Benavente, J.; Rodriguez-Castellon, E.; Palacio, L. J. J. o. c.; science, i. Effect of hydration of polyamide membranes on the surface electrokinetic parameters: surface characterization by X-ray photoelectronic spectroscopy and atomic force microscopy. **2002,** *247* (1), 149-158.
(43) Khorshidi, B.; Biswas, I.; Ghosh, T.; Thundat, T.; Sadrzadeh, M. J. S. r. Robust fabrication of thin film polyamide-TiO 2 nanocomposite membranes with enhanced thermal stability and anti-biofouling propensity. **2018,** *8* (1), 1-10.
(44) Tiraferri, A.; Kang, Y.; Giannelis, E. P.; Elimelech, M. Highly hydrophilic thin-film composite forward osmosis membranes functionalized with surface-tailored nanoparticles. *ACS applied materials & interfaces* **2012,** *4* (9), 5044-5053.
(45) Echlin, P.; Fiori, C.; Goldstein, J.; Joy, D. C.; Newbury, D. E. *Advanced scanning electron microscopy and X-ray microanalysis*, Springer Science & Business Media: 2013.
(46) Sadeghi, M.; Shamsabadi, A. A.; Ronasi, A.; Isfahani, A. P.; Dinari, M.; Soroush, M. Engineering the dispersion of nanoparticles in polyurethane membranes to control membrane physical and transport properties. *Chemical Engineering Science* **2018,** *192*, 688-698.
(47) Zhao, Q.; Hou, J.; Shen, J.; Liu, J.; Zhang, Y. Long-lasting antibacterial behavior of a novel mixed matrix water purification membrane. *Journal of Materials Chemistry A* **2015,** *3* (36), 18696-18705.
(48) Song, X.; Zhou, Q.; Zhang, T.; Xu, H.; Wang, Z. Pressure-assisted preparation of graphene oxide quantum dot-incorporated reverse osmosis membranes: antifouling and chlorine resistance potentials. *Journal of Materials Chemistry A* **2016,** *4* (43), 16896-16905.
(49) Xia, S.; Yao, L.; Zhao, Y.; Li, N.; Zheng, Y. Preparation of graphene oxide modified polyamide thin film composite membranes with improved hydrophilicity for natural organic matter removal. *Chemical Engineering Journal* **2015,** *280*, 720-727.
(50) Tang, C. Y.; Kwon, Y.-N.; Leckie, J. O. Effect of membrane chemistry and coating layer on physiochemical properties of thin film composite polyamide RO and NF membranes: II. Membrane physiochemical properties and their dependence on polyamide and coating layers. *Desalination* **2009,** *242* (1-3), 168-182.
(51) Kang, G.-d.; Cao, Y.-m. J. W. r. Development of antifouling reverse osmosis membranes for water treatment: a review. **2012,** *46* (3), 584-600.

(52) Asadollahi, M.; Bastani, D.; Musavi, S. A. Enhancement of surface properties and performance of reverse osmosis membranes after surface modification: a review. *Desalination* **2017,** *420*, 330-383.
(53) Al-Amoudi, A.; Lovitt, R. W. Fouling strategies and the cleaning system of NF membranes and factors affecting cleaning efficiency. *Journal of Membrane Science* **2007,** *303* (1-2), 4-28.
(54) Schwegmann, H.; Feitz, A. J.; Frimmel, F. H. J. J. o. c.; science, i. Influence of the zeta potential on the sorption and toxicity of iron oxide nanoparticles on S. cerevisiae and E. coli. **2010,** *347* (1), 43-48.
(55) Childress, A. E.; Elimelech, M. Effect of solution chemistry on the surface charge of polymeric reverse osmosis and nanofiltration membranes. *J Memb Sci.* **1996,** *119* (2), 253-268.
(56) Zhao, M.; Fu, S.; Zhang, H.; Huang, H.; Wei, Y.; Zhang, Y. Enhanced separation and antifouling performance of reverse osmosis membrane incorporated with carbon nanotubes functionalized by atom transfer radical polymerization. *RSC Advances* **2017,** *7* (74), 46969-46979.
(57) Tiraferri, A.; Yip, N. Y.; Straub, A. P.; Castrillon, S. R.-V.; Elimelech, M. A method for the simultaneous determination of transport and structural parameters of forward osmosis membranes. *Journal of membrane science* **2013,** *444*, 523-538.
(58) Phillip, W. A.; Yong, J. S.; Elimelech, M. Reverse draw solute permeation in forward osmosis: modeling and experiments. *Environmental science & technology* **2010,** *44* (13), 5170-5176.
(59) Zirehpour, A.; Rahimpour, A.; Seyedpour, F.; Jahanshahi, M. Developing new CTA/CA-based membrane containing hydrophilic nanoparticles to enhance the forward osmosis desalination. *Desalination* **2015,** *371*, 46-57.
(60) Lind, M. L.; Ghosh, A. K.; Jawor, A.; Huang, X.; Hou, W.; Yang, Y.; Hoek, E. M. Influence of zeolite crystal size on zeolite-polyamide thin film nanocomposite membranes. *Langmuir* **2009,** *25* (17), 10139-10145.
(61) Huang, H.; Ying, Y.; Peng, X. Graphene oxide nanosheet: an emerging star material for novel separation membranes. *Journal of Materials Chemistry A* **2014,** *2* (34), 13772-13782.
(62) Lee, S. Y.; Kim, H. J.; Patel, R.; Im, S. J.; Kim, J. H.; Min, B. R. Silver nanoparticles immobilized on thin film composite polyamide membrane: characterization, nanofiltration, antifouling properties. *Polymers for Advanced Technologies* **2007,** *18* (7), 562-568.
(63) Yin, J.; Yang, Y.; Hu, Z.; Deng, B. Attachment of silver nanoparticles (AgNPs) onto thin-film composite (TFC) membranes through covalent bonding to reduce membrane biofouling. *Journal of membrane science* **2013,** *441*, 73-82.
(64) Seyedpour, S. F.; Arabi Shamsabadi, A.; Khoshhal Salestan, S.; Dadashi Firouzjaei, M.; Sharifian Gh, M.; Rahimpour, A.; Akbari Afkhami, F.; Shirzad Kebria, M. r.; Elliott, M. A.; Tiraferri, A. Tailoring the Biocidal Activity of Novel Silver-Based Metal Azolate Frameworks. *ACS Sustainable Chem. Eng.* **2020**.
(65) Lu, X.; Ye, J.; Zhang, D.; Xie, R.; Bogale, R. F.; Sun, Y.; Zhao, L.; Zhao, Q.; Ning, G. Silver carboxylate metal–organic frameworks with highly antibacterial activity and biocompatibility. *J. Inorg. Biochem.* **2014,** *138*, 114-121.
(66) Berchel, M.; Le Gall, T.; Denis, C.; Le Hir, S.; Quentel, F.; Elléouet, C.; Montier, T.; Rueff, J.-M.; Salaün, J.-Y.; Haelters, J.-P. A silver-based metal–organic framework material as a 'reservoir'of bactericidal metal ions. *New J. Chem.* **2011,** *35* (5), 1000-1003.
(67) Wang, X.; Gao, W.; Xu, S.; Xu, W. Luminescent fibers: in situ synthesis of silver nanoclusters on silk via ultraviolet light-induced reduction and their antibacterial activity. *Chemical engineering journal* **2012,** *210*, 585-589.
(68) Rueff, J.-M.; Perez, O.; Caignaert, V.; Hix, G.; Berchel, M.; Quentel, F.; Jaffrès, P.-A. Silver-based hybrid materials from meta-or para-phosphonobenzoic acid: Influence of the topology on silver release in water. *Inorganic chemistry* **2015,** *54* (5), 2152-2159.
(69) Zhu, J.; Hou, J.; Zhang, Y.; Tian, M.; He, T.; Liu, J.; Chen, V. Polymeric antimicrobial membranes enabled by nanomaterials for water treatment. *Journal of Membrane Science* **2018,** *550*, 173-197.

(70) Chamakura, K.; Perez-Ballestero, R.; Luo, Z.; Bashir, S.; Liu, J. Comparison of bactericidal activities of silver nanoparticles with common chemical disinfectants. *Colloids Surf., B* **2011,** *84* (1), 88-96.
(71) Shen, L.; Zhang, X.; Zuo, J.; Wang, Y. Performance enhancement of TFC FO membranes with polyethyleneimine modification and post-treatment. *J Memb Sci.* **2017,** *534*, 46-58.